Chemical Engineering Journal 400 (2020) 125925

Contents lists available at ScienceDirect

Chemical Engineering Journal

journal homepage: www.elsevier.com/locate/cej

Construction of sugar-gourd-shaped CdS/$Co_{1-x}S$ hollow hetero-nanostructure as an efficient Z-scheme photocatalyst for hydrogen generation

Lei Li[a,1], Changfa Guo[a,1], Junling Shen[a], Jiqiang Ning[b], Yijun Zhong[a], Yong Hu[a,*]

[a] Key Laboratory of the Ministry of Education for Advanced Catalysis Materials, Department of Chemistry, Zhejiang Normal University, Jinhua 321004, China
[b] Vacuum Interconnected Nanotech Workstation, Suzhou Institute of Nano-Tech and Nano-Bionics, Chinese Academy of Sciences, Suzhou 215123, China

HIGHLIGHTS

- Sugar-gourd-shaped CdS/$Co_{1-x}S$ hollow hetero-nanostructure is constructed.
- Co-vacancy $Co_{1-x}S$ hollow polyhedron displays great potential for photocatalysis.
- Direct Z-scheme system enhances separation of photogenerated charge carriers.
- CdS/$Co_{1-x}S$ heterostructures exhibit the efficient photocatalytic H_2 generation.

ARTICLE INFO

Keywords:
CdS
$Co_{1-x}S$
Co vacancies
Z-scheme system
Photocatalytic H_2 production

ABSTRACT

Hollow hetero-nanostructures have unique advantages for energy storage and conversion and are highly desirable for their photocatalysis applications. We herein report the synthesis of an unusual sugar-gourd-shaped hollow hetero-nanostructure, $Co_{1-x}S$ hollow polyhedrons (HPs) skewered on CdS nanowires (NWs) (CdS/$Co_{1-x}S$ HHNSs), through a facile two-step strategy of growing ZIF-67 on CdS NWs followed by a sulfidation reaction. The loading amounts of $Co_{1-x}S$ HPs on an individual CdS NW can be adjusted by simply controlling the content of the $Co_{1-x}S$ precursor in the reaction. The coupling of the $Co_{1-x}S$ HPs with the CdS NWs not only broadens the solar light harvesting spectrum from ultraviolet to near infrared region, but also results in abundant Co vacancies as well as sides and facets with lots of active sites. More importantly, *in-situ* irradiated X-ray photoelectron spectroscopy confirms the direct Z-scheme transfer pathway of photogenerated charge carriers in the hetero-nanostructure, which facilitates the separation of photogenerated electron-hole pairs and induces strong photoreduction ability due to lower aligned conductor band of $Co_{1-x}S$. As a result, the gular-gourd-shaped CdS/$Co_{1-x}S$ HHNSs are demonstrated as an efficient visible light-driven photocatalyst for H_2 production. A H_2 production rate of 13.48 mmol g^{-1} h^{-1} is achieved with optimized CdS/$Co_{1-x}S$ HHNSs without using any additional co-catalyst. This is the first report on the performance of Co vacancies in $Co_{1-x}S$ hollow nanostructures for photocatalysis which inspire the development of unusual hollow hetero-nanostructures as efficient photocatalysts by means of morphology design and interfacial electronic modulation.

1. Introduction

Converting solar energy into chemical energy (such as H_2) with semiconductors by the means of photocatalysis is an appealing and promising solution to address the ever-increasing energy crisis and environmental issues [1–3]. Since the pioneering report on photocatalytic water splitting in 1972, a large number of semiconductor photocatalysts have been developed to enhance the solar-to-chemical (STC) efficiency [4–9]. Despite great progresses have been made, the STC efficiency is still unsatisfactory and further improvement is still needed. A major obstruction of STC efficiency lies in the incongruous photocatalytic systems where the recombination of electrons (e^-) and holes (h^+) in a semiconductor occurs in picoseconds, while the migration of charge carriers to surface and the reaction at surface take microseconds and milliseconds, respectively [10,11]. Therefore, to achieve high photocatalytic activity, it is crucial to boost surface

* Corresponding author.
E-mail address: yonghu@zjnu.edu.cn (Y. Hu).
[1] These authors contributed equally to this work.

https://doi.org/10.1016/j.cej.2020.125925
Received 25 March 2020; Received in revised form 12 June 2020; Accepted 13 June 2020
Available online 17 June 2020
1385-8947/

reactions and further promote photoelectric efficiency.

The photoelectric efficiency is associated with the migration and transfer of photogenerated charge carriers, which rely on the composition and electronic band structure of a photocatalyst. For an individual semiconductor, the photoelectric efficiency is generally low due to the limited migration and transfer of photogenerated carriers [12]. A constructed heterostructure has been proved to be effective to facilitate the separation and transfer of charge carriers from one semiconductor to the other through the coupled interface [13]. The electron transfer pathways in heterogeneous photocatalysts are categorized into three groups in terms of band alignment, Type-I, Type-II and Z-scheme, among which the Z-scheme transfer is the most efficient in separating charge carriers and enhancing photoelectric efficiency [12]. In addition to the electronic band configuration, the architecture of heterostructures influences the efficiency of photoelectrical conversion as well. It has been suggested that the hetero-nanostructure is more effective in photoelectrical conversion as it offers an extremely high surface area while maintaining an interconnected network to ensure the excellent charge carrier conduction [14–17]. However, the construction of hollow hetero-nanostructures with direct Z-scheme band alignment with usual inorganic semiconductors is still challenging.

Hollow nanostructures exhibit the unique advantage of larger exposed surface which effectively accelerates surface reactions [18,19]. For instance, hollow nanospheres show higher photocatalytic activity towards CO_2 reduction reaction (CRR) and H_2 evolution reaction (HER) than the solid counterparts owing to enhanced light harvesting due to multiple scattering/reflection of light and larger specific surface area offering more active sites for surface reactions [20–22]. Compared with hollow spheres, the hollow cubes show further enhanced catalytic activity because of the anisotropic shape of the cubic morphology and more exposed sides and facets as active sites [21]. These advantages exert to the greatest extent in the hollow polyhedrons (HPs) which exhibit efficient photocatalytic performance for HER, CRR, and so on [23,24]. Thus, introducing HPs into a Z-scheme heterostructure can substantially improve photocatalytic activity by virtue of enhanced sunlight harvesting and expedited surface reactions.

Recently, metal chalcogenides have attracted wide attention and become an important research topic due to their unique electronic band structure [21,23,24]. As a typical example, cobalt sulfides (CoS_x) have the following merits as the photocatalyst: narrow band gap for visible light response, high flat-band potential with strong photoreduction ability, and efficient charge transfer through intermediate sulfur atoms bonded to the metal atoms at interface [21]. Hence, the CoS_x-based heterostructures such as Co_9S_8@$ZnIn_2S_4$ and CdS/Co_9S_8 exhibit excellent performance for photocatalytic H_2 production [21,23]. In these heterostructures, the S vacancies in CoS_x generally act as active sites and play important roles in adsorbing and activating insert molecules. In contrast, the Co vacancies in $Co_{1-x}S$ for photocatalysis earn less concern, although they are important for advanced electrodes for various batteries, electrocatalysis and supercapacitors in the previously reported studies [25–27].

Herein, a sugar-gourd-shaped direct Z-scheme hollow hetero-nanostructure of $Co_{1-x}S$ HPs skewered on CdS nanowires (NWs) (CdS/$Co_{1-x}S$ HHNSs) is synthesized through a two-step strategy of growing ZIF-67 on CdS NWs followed by a facile sulfidation reaction. The obtained CdS/$Co_{1-x}S$ HHNSs are an efficient visible light-driven photocatalyst for hydrogen production. The H_2 production rate of 13.48 mmol g^{-1} h^{-1} is achieved with optimized CdS/$Co_{1-x}S$ HHNSs without using any additional co-catalyst. The remarkable photocatalytic activity is attributed to the coupling of CdS NW and $Co_{1-x}S$ HPs, which endows the CdS/$Co_{1-x}S$ HHNSs with broad light spectrum response and large specific surface area to expose abundant sides and facets with active sites. More importantly, the Z-scheme carrier transfer mechanism substantially facilitates the separation of photogenerated e^--h^+ pairs, leaving photoexcited electrons in the conduction band (CB) of $Co_{1-x}S$ HPs and thus leading to strong photoreduction ability. This work demonstrates the potential of direct Z-scheme hollow hetero-nanostructure of $Co_{1-x}S$ with Co vacancies as an efficient photocatalyst for hydrogen production.

2. Experimental section

2.1. Material preparation

Synthesis of CdS NWs: CdS NWs were synthesized via a solvothermal method [28]. Briefly, 0.855 g of $Cd(NO_3)_2{\cdot}4H_2O$ and 0.630 g of thiourea were dissolved in 22.5 mL of ethanediamine. The resulting solution was transferred into a 45 mL Teflon-lined stainless-steel autoclave and then kept at 180 °C for 24 h. After cooled down to room temperature, the bright yellow precipitate was collected by centrifugation and washed with deionized water and absolute ethanol for several times to remove impurities. Finally, the product was dried at 60 °C for 12 h.

Synthesis of ZIF-67: 1.313 g of 2-methylimidazolem (2-MI) and 0.582 g of $Co(NO_3)_2{\cdot}6H_2O$ were dissolved in 20 mL of methanol, respectively. Then, the solution of 2-MI was quickly poured into the solution of $Co(NO_3)_2{\cdot}6H_2O$ followed by stirring violently for 5 min. The resultant mixed solution was aged for 10 min at room temperature. Finally, the purple precipitate was collected by centrifugation and washed with absolute ethanol for several times and dried at 60 °C for 12 h.

Synthesis of sugar-gourd-shaped CdS/ZIF-67 hybrids: 0.388 g of Co$(NO_3)_2{\cdot}6H_2O$ and 0.050 g of CdS NWs were dispersed in 20 mL of methanol with the assistance of sonication for 5 min, and the obtained dark yellow mixture was denoted as solution A. 0.875 g of 2-MI and 20 mL methanol were mixed to obtain solution B. Afterward, solution B was rapidly transferred into solution A under vigorous magnetic stirring for 5 min. The resultant mixed solution was aged for 10 min at room temperature. Finally, the precipitates (denoted as CdS/ZIF-67-2) were collected by centrifugation and washed with absolute ethanol for three times, then dried at 60 °C for 12 h. For comparison, the same method was employed to synthesize CdS/ZIF-67-1 with 0.194 g $Co(NO_3)_2{\cdot}6H_2O$ and 0.438 g 2-MI, and CdS/ZIF-67-3 with 0.582 g $Co(NO_3)_2{\cdot}6H_2O$ and 1.313 g 2-MI.

Synthesis of sugar-gourd-shaped CdS/$Co_{1-x}S$ HHNSs: In a typical procedure, 0.080 g of thioacetamide (TAA) and 0.080 g of the as-prepared sugar-gourd-shaped CdS/ZIF-67-x (x = 1, 2, 3) were dispersed in 27 mL of absolute ethanol with the assistance of sonication for 3 min, and the mixture was transferred into a 45 mL Teflon-lined stainless steel autoclave and kept at 120 °C for 4 h. After cooled to room temperature, the product was collected by centrifugation and washed with deionized water and absolute ethanol for several times to remove impurities. Finally, the precipitate was dried at 60 °C for 12 h. The products prepared with CdS/ZIF-67-x are in correspondence with CdS/$Co_{1-x}S$-n (n = 1, 2, 3), which are denoted as CCS-1, CCS-2, and CCS-3 HHNSs, respectively. In addition, the CdS/CoS sample is also prepared using the same method with 0.050 g CdS NWs, 0.0668 g $Co(NO_3)_2{\cdot}6H_2O$, and 0.0172 g TAA, and 27 mL of absolute ethanol.

Synthesis of $Co_{1-x}S$ HPs: 0.080 g of ZIF-67 and 0.080 g of TAA were dispersed in 27 mL of ethyl alcohol. Then the solution was transferred into a 45 mL Teflon-lined stainless-steel autoclave and kept at 120 °C for 4 h. After cooled down to room temperature, the black precipitate was collected by centrifugation and washed with deionized water and absolute ethanol for several times to remove impurities, and dried at 60 °C for 12 h.

2.2. Sample characterizations

The crystal structure and phase purity of the samples were characterized by Powder X-ray diffractometer (XRD) measurements performed with a Philips PW 3040/60 XRD using the Cu Kα radiation. The morphologies were viewed with a field-emission scanning electron microscope (FESEM) with the assistance of a Hitachi S-4800 scanning

electron micro-analyzer. The transmission electron microscopy (TEM), high-resolution TEM (HRTEM), and scanning transmission electron microscopy energy-dispersive X-ray spectroscopy (STEM-EDS) mapping analysis were carried out on a JEOL JEM-2100F microscope with an accelerating voltage of 200 kV. N_2 adsorption and desorption isotherms were obtained at 77 K on a surface area and porosimetry analyzer V-Sorb 2800P, with samples degassed in vacuum at 100 °C for 4 h. The surface composition and chemical state of the samples were analyzed with X-ray photoelectron spectroscopy (XPS), using an ESCALab MKII X-ray photoelectron spectrometer with Mg Kα X-ray as the excitation source. Photoluminescence (PL) spectra were acquired using a FLS 920 fluorescence spectrophotometer with an excitation wavelength of 380 nm. The surface photocurrent measurements were carried out at room temperature on a surface photovoltage spectrometer (PLSPS/IPCE1000 Beijing Perfect light technology Co., Ltd.) consisting of a source of monochromatic light with a mechanical chopper (SR 540, Stanford research, Inc.) and a lock-in amplifier. UV–vis diffuse reflectance spectra (UV–vis DRS) of the samples were recorded over the range of 200–800 nm with the absorption mode of a Thermo Nicolet Evolution 500 UV–vis spectrophotometer equipped with an integrating sphere attachment. Raman measurements were performed using a Renishaw inVia RM10000 micro-Raman spectrometer (λ = 514.5 nm).

2.3. Electrochemical and photoelectrochemical measurements

The Mott-Schottky measurements were performed at different frequencies (200, 500, 800 Hz) with an ac voltage of 10 mV and various applied potentials on a Zennium E station (ZAHNER, Germany) which works with a standard three-electrode cell with 0.5 M Na_2SO_4 as the electrolyte solution in a three electrode quartz cell, the glassy carbon electrode covered with photocatalyst as the working electrode, a platinum wire as the counter electrode, and saturated calomel electrode (SCE) as the reference electrode. Electrochemical impedance spectroscopy (EIS) measurements were also carried out in a $K_3[Fe(CN)_6]$ (5 mM) and KCl (1 M) aqueous solution with the Zennium E station, at frequencies ranging from 0.1 Hz to 100 kHz with an ac voltage of 10 mV. Photocurrent measurements under visible-light irradiation were performed at the 0.2 V bias potential vs. SCE on a CHI840C electrochemical workstation (Chenhua Instrument, China) with a standard three-electrode configuration using phototcatalyst-precoated fluorine doped tin oxide (FTO) (coated area: 1 cm^2) as the working electrode, Pt wire as the counter electrode, SCE as the reference electrode, and 0.5 M Na_2SO_4 aqueous solution as the electrolyte. A Xe lamp with a cut-on filter (λ > 420 nm) was employed as the visible light source. 5 mg of sample was add to the mixed solution of 50 μL of ethanol and 10 μL of Nafion solution (5 wt%) under sonication, then 15 μL of mixture ink was pipetted on the surface of a FTO glass to obtain a coating films of 1 × 1 cm^2 large.

2.4. Photocatalytic H_2 production measurement

Photocatalytic H_2 production: The photocatalytic H_2 evolution reaction was conducted on a Labsolar-III AG system with a Pyrex reaction vessel connected to an online gas chromatograph (Agilent Technologies GC-7890B, TCD, Ar carrier). The photocatalytic reaction was evaluated in a gas-closed reactor connecting to a water bath to maintain the reaction temperature at 25 °C. In a typical reaction, 20 mg of photocatalysts was dispersed in 100 mL of aqueous solution containing 20% lactic acid as the sacrificial agents. Before performing the photocatalytic experiments, the reaction vessel was purged with argon and evacuated for at least 30 min to remove dissolved air. The suspension was irradiated by a 300 W Xe lamp (MicroSolar 300, Perfect Light) equipped with an optical filter at 420 nm to cut off the ultraviolet light.

The AQE for photocatalytic H_2 production: The AQE of photocatalytic H_2 production was calculated according to Eq. (1):

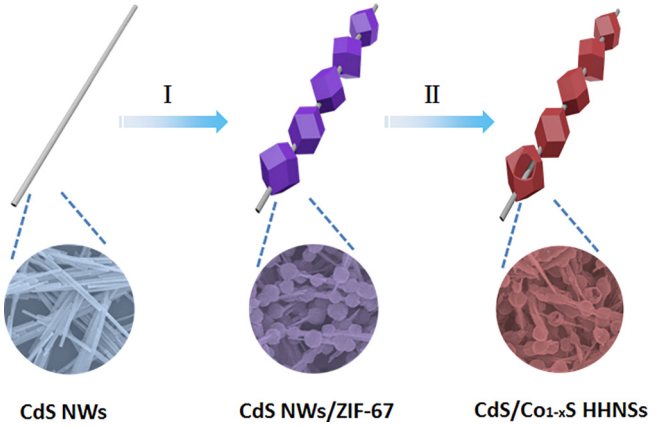

Fig. 1. Schematic illustration of the synthetic process of the sugar-gourd-shaped CdS/Co_{1-x}S HHNSs.

$$AQE = \frac{N_e}{N_p} = \frac{N_{H_2} \times 4}{N_p} = \frac{n_{H_2} \times N_A \times 4}{\frac{W \times A \times t}{h \times \nu}} \times 100\% \quad (1)$$

where N_e, N_p and N_A represent the number of reacted electrons, incident photons and generated hydrogen, respectively, n_{H_2}represents the molar number of generated hydrogen, ν, W, A and t are the incident light frequency, intensity, irradiation area and time, respectively, and N_A and h are the Avogadro's constant and Planck constant, respectively.

3. Results and discussion

The two-step synthesis strategy of the sugar-gourd-shaped CdS/Co_{1-x}S HHNSs is shown in Fig. 1. The CdS NWs are first prepared according to the previously reported method [28], and the selection of CdS as a constituent is motivated by its advantageous properties for photocatalysis, such as a suitable band gap and the adjustable band edge position [29–32]. The ZIF-67 polyhedrons are then synthesized with the presence of CdS NWs, achieving the interesting sugar-gourd-shaped hybrid nanoarchitecture of CdS/ZIF-67, polyhedron structures skewered on the CdS NWs, which is the precursor of CdS/Co_{1-x}S HHNSs (step I). The sugar-gourd-shaped CdS/Co_{1-x}S HHNSs are finally obtained by a mild sulfidation reaction of CdS/ZIF-67 with TAA at 120 °C for 4 h (step II), where the ZIF-67 polyhedrons are directly transformed into Co_{1-x}S HPs on the CdS NWs.

The morphology and phase composition of the sugar-gourd-shaped CdS/Co_{1-x}S HHNSs were examined by FESEM and TEM in combination with the XRD technique. The FESEM images in Fig. 2a and b show that the obtained CdS NWs have a size of ca. 50 nm in diameter and ca. 5 μm in length. The mechanical stability of the NW enables the skewering of the ZIF-67 polyhedrons to obtain the sugar-gourd-shaped hybrid structures. As shown in Fig. 2c, the morphology of the as-prepared CdS/ZIF-67 hybrids exhibits the obvious sugar-gourd shape, indicating that the ZIF-67 polyhedrons are successfully skewered on the CdS NWs. The skewered gourds present a polyhedral morphology with a smooth surface and a diameter of ca. 450 nm (Fig. 2d). The XRD pattern shows the product consists of the pure ZIF-67 phase and hexagonal-phase CdS (JCPDS No. 41-1049) (Fig. S1). After sulfidation reaction, the resulting CdS/Co_{1-x}S HHNSs (the mass ratio of $Co(NO_3)_2{\cdot}6H_2O$, 2-MI and CdS NWs is 388: 875: 50, respectively, denoted as CCS-2) maintain the sugar-gourd-shaped morphology (Fig. 2e), whereas the high-magnification FESEM image reveals the rough surface of the CCS-2 HHNSs, especially for the polyhedral gourds (Fig. 2f). Moreover, the cracked gourds indicated by red arrows imply that the solid polyhedrons are directly transformed into hollow structure through this *in-situ* sulfidation treatment.

Fig. 3a shows the TEM images of the as-prepared CCS-2 HHNSs, which further confirms that all the solid ZIF-67 polyhedrons are

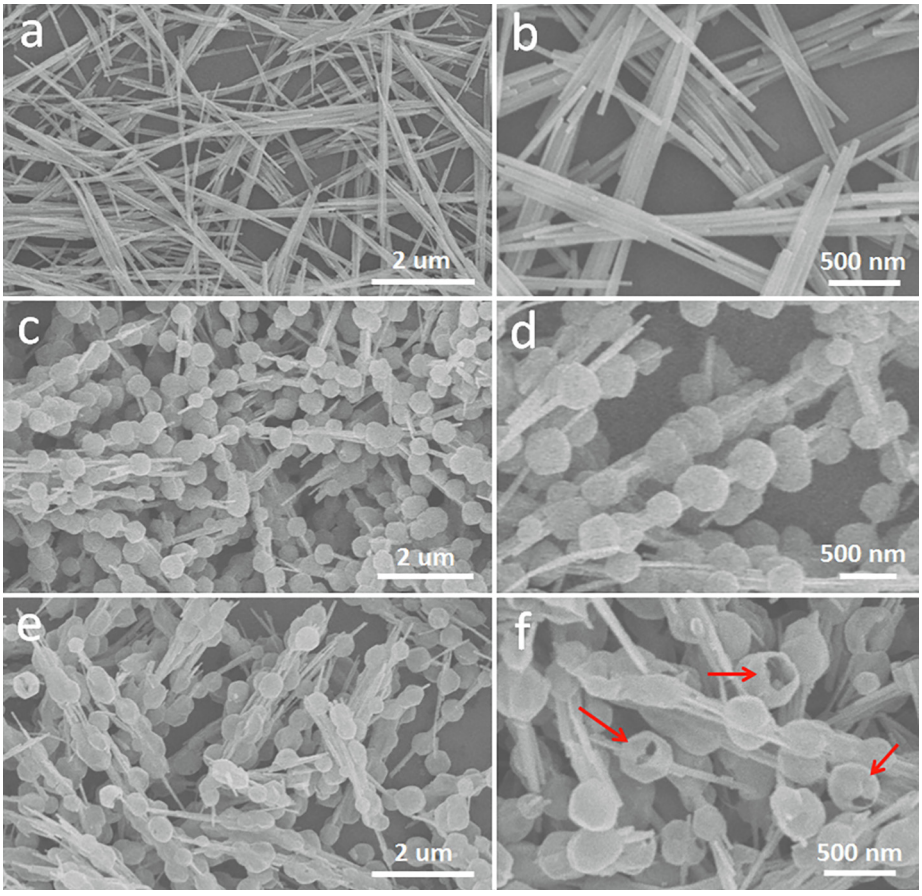

Fig. 2. FESEM images of the as-prepared (a, b) CdS NWs, (c, d) CdS/ZIF-67 hybrids, (e, f) CCS-2 HHNSs.

completely converted into hollow structures on CdS NWs. Revealed by the high-magnification TEM image (Fig. S2), each HP is composed of numerous fine nanoparticles (ca. 6 nm). The XRD pattern of the CCS-2 HHNSs shows all the diffraction peaks can be assigned to the sole hexagonal phase of CdS (Fig. S3), also implying the form of ultrasmall nanocrystals of the $Co_{1-x}S$ HPs [33]. The HRTEM image in Fig. 3b, taken from the side surface of an individual CCS-2 HHNS marked with a yellow ring in Fig. 3a, displays the tight interfacial contract between

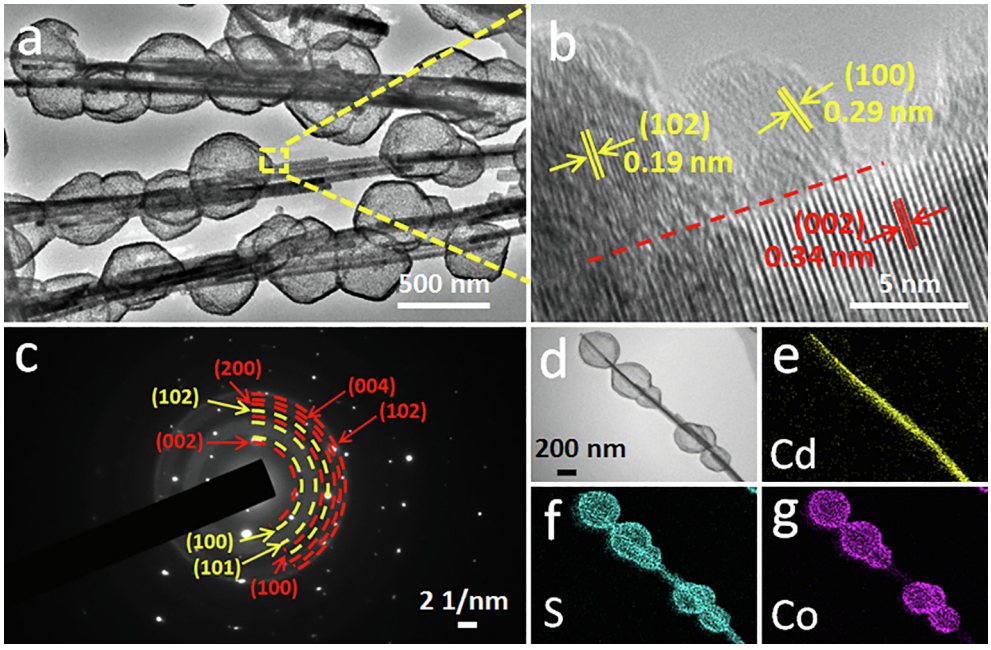

Fig. 3. (a) TEM, (b) HRTEM, (c) corresponding SAED pattern of the as-prepared CCS-2 HHNSs, (d) STEM, and STEM-EDS elemental mapping images for (e) Cd, (f) S, and (g) Co elements of individual CCS-2 HHNS.

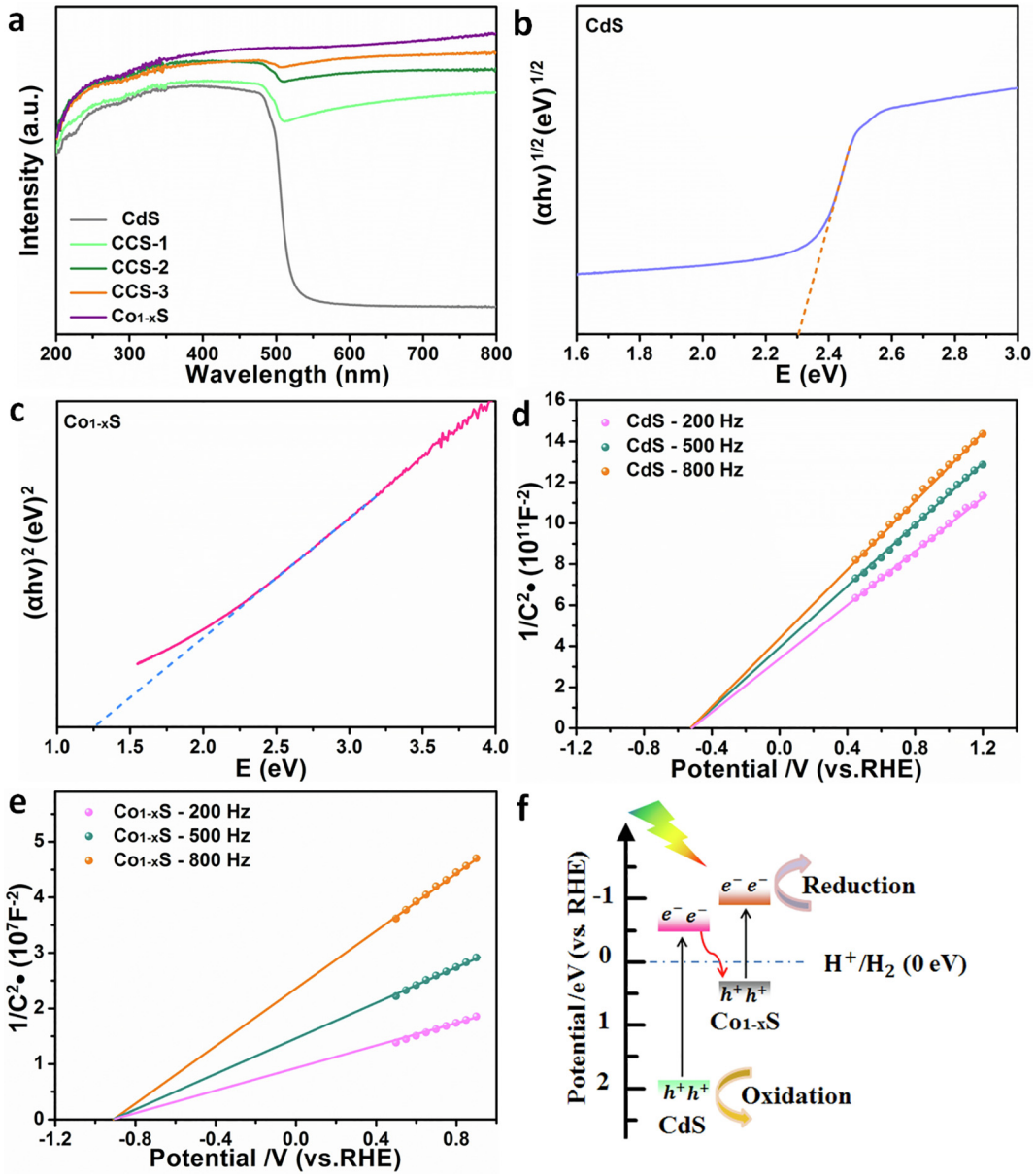

Fig. 4. (a) UV–vis DRS of the as-prepared different samples. Tauc plots of (b) CdS NWs and (c) $Co_{1-x}S$ HPs. Mott-Schottky plots of (d) CdS NWs and (e) $Co_{1-x}S$ HPs. f) Schematic illustration for the band configuration and favored charge transfer pathway in the CCS HHNSs.

CdS NW and $Co_{1-x}S$ HP which is expected to favor the charge transfer across the interface. Separated by the interface, the lattice fringes exhibit a spacing of 0.34 nm in the NW, in good agreement with the d value of the (002) plane of hexagonal phase CdS [28], and those spacing of 0.19 and 0.29 nm of the nanoparticles in a HP can be indexed to the (102) and (100) plane of hexagonal phase $Co_{1-x}S$, respectively (JCPDS No. 42-0826). The selected area electron diffraction (SAED) pattern (Fig. 3c) clearly reveals the existence of CdS (red) and Co-deficiency $Co_{1-x}S$ (yellow) phases in the product. The STEM-EDS elemental mapping images of individual CCS-2 HHNS signify that the existence and uniform distribution of Cd, S, and Co elements within the HPs and NW, respectively (Fig. 3d-g). These results together demonstrate the successful synthesis of sugar-gourd-shaped CdS/$Co_{1-x}S$ HHNSs. N_2 adsorption-desorption isotherm is employed to assess the Brunauer-Emmett-Teller (BET) specific surface area of the CCS-2 HHNSs (Fig. S4). It is found that the CCS-2 HHNSs possess a surface area of 47.96 $m^2\ g^{-1}$, which is high for inorganic nanostructures and can exposes lots of active sites to accelerate surface reactions. Furthermore, the corresponding pore size distribution curve demonstrates the existence of mesopores in the $Co_{1-x}S$ HPs, which can facilitate the mass transfer in heterogeneous catalysis (inset of Fig. S4). Although the limited interfacial contact may impede the photoelectrical efficiency somewhat. Considering the $Co_{1-x}S$ HPs possess many sides and facets with lots of active sites and that the surface reaction is the rate-determined step for photocatalysis, the enhanced photocatalytic activity is expectable.

To explore the formation mechanism of the sugar-gourd-shaped CdS/$Co_{1-x}S$ HHNSs, we investigated the evolution of morphology and structure of the CdS/ZIF-67 hybrids with the reaction time. The FESEM images of the as-prepared CdS/ZIF-67 hybrids obtained at different intervals are shown in Fig. S5. First, some Co^{2+} ions can be absorbed on the surface of CdS NWs in solution A, offering the nucleation sites for ZIF-67 nanoparticles. Upon the concentration of Co^{2+} and 2-MI in reaction system is increased, and the nucleation of the ZIF-67 nanoparticles is predominated at the early stage (Fig. S5a). As the concentration of Co^{2+} and 2-MI gradually decreases with the reaction time, the transformation from the nucleation-dominated to growth-dominated process occurs, accompanied by the formation of some larger ZIF-

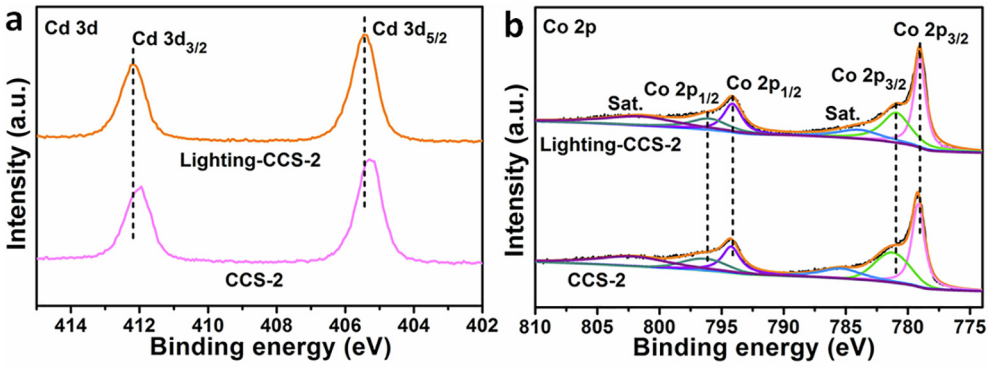

Fig. 5. XPS high-resolution spectra of the CCS-2 HHNSs with and without light irradiation: (a) Cd 3d and (b) Co 2p.

67 nanoparticles on CdS NWs (Fig. S5b). With reaction time prolonging, the growth of ZIF-67 particles became dominated, corresponding to the irregular polyhedral morphology (Fig. S5c). After 10 min, the concentration of Co^{2+} and 2-MI in reaction system is low enough, the growth process of ZIF-67 finish with the formation of ZIF-67 polyhedrons skewered on the CdS NWs (Fig. S5d). Finally, the sugar-gourd-shaped CdS/Co_{1-x}S HHNSs were obtained by a mild sulfidation reaction of CdS/ZIF-67 with TAA at 120 °C for 4 h, where the ZIF-67 polyhedrons were directly transformed into Co_{1-x}S HPs on the CdS NWs.

Interestingly, the loading amounts of Co_{1-x}S HPs on an individual CdS NW can be tuned by changing the ratio of ZIF-67 precursor and CdS NWs in the sulfidation treatment. When the ratio is lower than that of CCS-2 HHNSs, the loading content of Co_{1-x}S HPs is reduced and more surface of the CdS NWs (denoted as CCS-1) is exposed (Fig. S6a and b). In contrast, a higher loading of Co_{1-x}S HPs on the CdS NWs can be obtained with the increasing of the ratio of ZIF-67, and therefore less surface of the CdS NWs is exposed accordingly (denoted as CCS-3) (Fig. S6c and d). Using the hetero-nanostructure as a photocatalyst, the sufficient exposure of the surface is significant for enhanced photocatalytic activity in terms of light harvesting and synergistic effect. For comparison, Co_{1-x}S HPs were prepared from ZIF-67 polyhedrons without the presence of CdS NWs (Fig. S6e and f). The composition and constitution of the four samples above are further confirmed by the FESEM-EDS analysis (Fig. S7). Moreover, the ratio of Co and S for all the as-prepared samples are basically unchanged after deducting the proportion of S coordinated with CdS, (about 0.7), indicating the presence of abundant Co vacancies in Co_{1-x}S. To further support the presence of Co vacancies in Co_{1-x}S HPs, Raman spectra of the CCS-2 HHNSs, Co_{1-x}S HPs, and CdS/CoS hybrids are presented in Fig. S8. Compared with CdS/CoS, a redshift and broadening appeared in the vibration modes for the CdS/Co_{1-x}S HHNSs and Co_{1-x}S HPs, further verifying the presence of Co vacancy [34]. The Co vacancies would change local atomic configuration and thus modulate the electronic structure, and act as active sites as well to adsorb and activate inset molecules and facilitate the catalytic processes [34,35].

The electronic band structure of the CCS HHNSs is examined by UV–vis DRS and Mott-Schottky measurements. The UV–vis DRS shows that the CdS NWs only absorb the light of wavelength below about 530 nm (Fig. 4a), while the Co_{1-x}S HPs exhibit strong full-spectrum absorption due to multiple scattering/reflection of light in the hollow structure. Benefiting from the introduction of Co_{1-x}S HPs, all the CCS HHNSs broaden solar light absorption from the ultraviolent to near infrared region in comparison with CdS NWs, giving a full spectrum response. Such improvement enables the HHNSs to substantially utilize visible light to drive chemical reactions. Moreover, the band gaps (E_g) of two semiconductors are determined from the corresponding Tauc plots to be 2.30 eV for CdS NWs and 1.25 eV for Co_{1-x}S HPs (Fig. 4b and c) [36]. Such band configuration makes the two semiconductors meet the primary requirement for constructing a Z-scheme system: $E_g < 3$ eV [37]. The Mott-Schottky plots reveal the derived flat-band potential of the Co_{1-x}S HPs is −0.90 eV versus the reversible hydrogen electrode (RHE) potential, more negative than that of CdS (−0.50 eV vs. RHE) (Fig. 4d and e). The CB energy (E_{CB}) of both the semiconductors are determined accordingly. The valence band (VB) energy (E_{VB}) of Co_{1-x}S HPs and CdS NWs were calculated from $E_{CB} + E_g$ and located at 0.35 and 1.80 eV (vs. RHE), respectively. The energy band alignment (vs. RHE) is schematically illustrated in Fig. 4f. According to the band configuration of the CCS HHNSs, the interfacial charge transfer takes place in the direct Z-scheme pathway under light irradiation. In addition, low E_g indicates high conductivity of Co_{1-x}S HPs relative to CdS NWs. That is, the photoelectrons can be transferred from CdS to Co_{1-x}S, which participates the surface reactions.

To elucidate the interfacial charge transfer mechanism in the CSS HHNSs under irradiation, *in-situ* irradiated XPS is employed to accurately reflect the charge transfer pathway [38,39]. Without light irradiation, the XPS survey spectrum of the as-prepared CCS-2 HHNSs confirms the existence of Cd, Co and S elements in the heterostructures (Fig. S9). The atomic rate of Co and S is determined to be about 0.6 for Co_{1-x}S, lower than that (0.7) by FESEM-EDS, implying most Co vacancies are located at the (sub-)surface of the HPs. The Cd 3d high-resolution spectrum shows two symmetry peaks at 411.9 and 405.2 eV, which correspond to Cd $3d_{5/2}$ and $3d_{3/2}$, respectively, being the signature of Cd^{2+} (Fig. 5a) [38]. In contrast, the XPS high-resolution spectrum of Co 2p orbital region displays several asymmetry peaks, which can be deconvoluted into three components: Co $2p_{3/2}$ and $2p_{1/2}$ at 779.1 and 794.2 eV from Co^{3+}, Co $2p_{3/2}$ and $2p_{1/2}$ at 781.2 and 796.3 eV from Co^{2+}, and satellite peaks, respectively (Fig. 5b) [21,40]. The co-existence of Co^{3+} and Co^{2+} corresponds to the identification of Co_{1-x}S by the SAED, HRTEM and FESEM-EDS analysis, demonstrating further the existence of Co vacancy. With light irradiation, the CCS-2 HHNSs show similar Cd 3d and Co 2p XPS high-resolution spectra to the samples without irradiation, while some obvious shifts in binding energy can be observed. All Cd 3d peaks are shifted towards higher binding energies (by + 0.2 eV), indicating reduced electron density for CdS NWs. In contrast, all the peaks of Co 2p are shifted to lower binding energy (by −0.1 eV for Co^{3+}, by −0.3 eV for Co^{2+}), signifying the increased electron density on Co_{1-x}S HPs. By contrast, there are hardly change in binding energy observed for the pure CdS NWs and Co_{1-x}S HPs with/without light irradiation, respectively (Fig. S10). Taken together, it can be concluded that the electrons are excited from the VB to CB of CdS under irradiation, and then transfer to Co_{1-x}S across the interface of two semiconductors to combine with h^+, confirming the Z-scheme system rather than the type-II transfer pathway.

Upon confirming the advantages of the CdS/Co_{1-x}S HHNSs on photocatalysis, we employed the photoreduction reaction of H_2O as the model reaction to assess the catalytic activity of the as-prepared HHNSs. The photocatalytic H_2 production test was conducted under visible-light irridation in 100 mL of aqueous solution containing 20% lactic acid as the sacrificial agent. Fig. 6a compares the photocatalytic H_2 production activity of CCS-1, CCS-2, and CCS-3 HHNSs, bare Co_{1-x}S

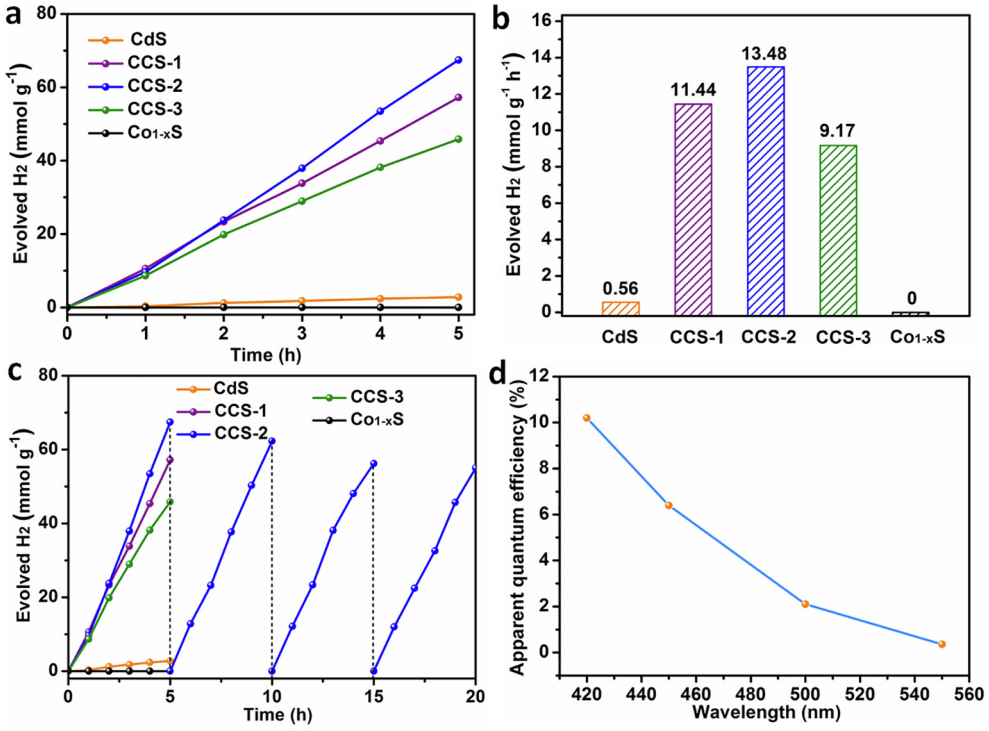

Fig. 6. (a) Typical time course of H_2 production catalyzed by CdS NWs, $Co_{1-x}S$ HPs, CCS-1, CCS-2, and CCS-3 HHNSs, Light irradiation conditions: visible light ($\lambda > 420$ nm), 100 mW cm^{-2}, lactic acid as the sacrificial agent. (b) Photocatalytic H_2 evolution rates on various samples in the first 5 h. (c) Cyclic tests of the photocatalytic H_2 production over the CCS-2 HHNSs. (d) Calculated AQEs for H_2 production over the CCS-2 HHNSs under monochromatic light irradiation.

HPs, and CdS NWs. Obviously, the photocatalytic H_2 production rate of all the as-prepared HHNSs significantly outperforms that of single-component catalysts. In particular, the CCS-2 HHNSs achieve a H_2 production rate of 13.48 mmol g^{-1} h^{-1}, 24-fold higher than that of CdS NWs (0.56 mmol g^{-1} h^{-1}) (Fig. 6b). The enhanced catalytic activity can be rationalized in terms of high specific surface area, the exposure of lots of sides, facets and Co vacancies on HPs, as well as the Z-scheme transfer pathway of photoexcited charge carriers [21]. However, less or more loading of $Co_{1-x}S$ in the hetero-nanostructure (CCS-1 or CCS-3 HHNSs) would induce negative effects on the photocatalytic activity, resulting in a reduced rate of H_2 production. Such reduction may be ascribed to the insufficient exposure of CdS NWs, which impedes the light absorption ability of the HHNSs and thus retards the process of interfacial charge transfer. In addition, we further assess another crucial parameter for photocatalysis, durability. As shown in Fig. 6c, the high H_2 production rate is well maintained during four cyclic tests with each run for 5 h. The sample characterizations after cyclic tests show the CCS-2 HHNSs retain the hollow sugar-gourd-shaped morphology (Fig. S11) and unchanged phase composition (Fig. S12a), indicating high structural stability and good reusability. The XPS survey spectra of the CCS-2 NNHSs before and after photocatalytic tests display a similar profile (Fig. S12b). Furthermore, the high-resolution XPS spectra of Cd 3d and Co 2p show no obvious shift in binding energy as well (Fig. S12c and d). Taken together, it can be concluded that the CCS-2 HHNSs exhibit the excellent chemical stability in the photocatalytic process. To evaluate the light utilization efficiency, the wavelength-dependent AQEs of the CCS-2 HHNSs are determined by measuring the amount of generated H_2 under various monochromatic light irradiation (Fig. 6d). The AQE at 420 nm is determined to be 10.2%, which is also comparable to previously reported photocatalysts (Table S1). To our best knowledge, this is the first demonstration of the superior photocatalytic H_2 generation with $Co_{1-x}S$-based HHNSs which can be a promising candidate for photocatalytic water reduction.

To further confirm the Z-scheme transfer mechanism and thus enhanced photocatalytic performance, we performed a series of photoelectrochemical and electrochemical measurements with the as-prepared CCS HHNSs and bare CdS NWs. Fig. 7a displays the PL spectra of these samples. It is clear that the bare CdS NWs show a strong PL emission at about 520 nm, while combined with $Co_{1-x}S$ HPs, the PL intensity are remarkably reduced for all heterostructures. The reduction suggests the introduction of $Co_{1-x}S$ HPs changes the electron transfer pathway across the interface and thus reduces the recombination kinetics of photogenerated charge carriers [41]. The CCS-2 HHNSs exhibit the weakest PL intensity among three heterostructures, confirming the importance of moderate $Co_{1-x}S$ loading on individual CdS NW for substantially promoting the photoelectrical conversion efficiency. This can be verified further by the surface photocurrent (SPC) response in terms of the light wavelength characterized by surface photocurrent spectrum (Fig. 7b) [42]. All samples only display the SPC signal below about 530 nm, corresponding to the requirement of simultaneous excitation of both semiconductors in the Z-scheme system. However, all the HHNSs display remarkably enhanced SPC as compared with CdS NWs. In particular, the highest value is achieved with the CCS-2 HHNSs, demonstrating the best photoelectrical efficiency. Under visible-light radiation, a similar trend of current density over the four samples is also observed (Fig. 7c). The CCS-2 HHNSs give the highest current density among four samples, suggesting the best separation efficiency of e^--h^+ pairs [43]. Moreover, the enhanced photocurrent response can reproducibly increase under each photoirradiation and quickly recover in the dark. Furthermore, we perform the EIS measurements to examine the interfacial charge transfer kinetics [44,45]. The diameter of the semi-circle in a Nyquist plot is proportional to the charge-transfer resistance of a sample, providing valuable information on charge transfer processes. As shown in Fig. 7d, the semi-circular Nyquist plots have the largest diameter for CdS NWs, but display significantly decreased diameters for all the CCS HHNSs especially with the smallest diameter for the CCS-2 sample, implying the charge-transfer barrier is reduced mostly in the HHNSs. In particularly, the fitting results from EIS illustrate the CCS-2 HHNSs possess the lowest charge transfer resistance (R_{ct}) among all the heterostructures (Table S2), which further confirms the fast electron transfer kinetics and thus efficient separation of photogenerated e^--h^+ pairs.

4. Conclusion

In summary, we have synthesized a sugar-gourd-shaped CdS/$Co_{1-x}S$

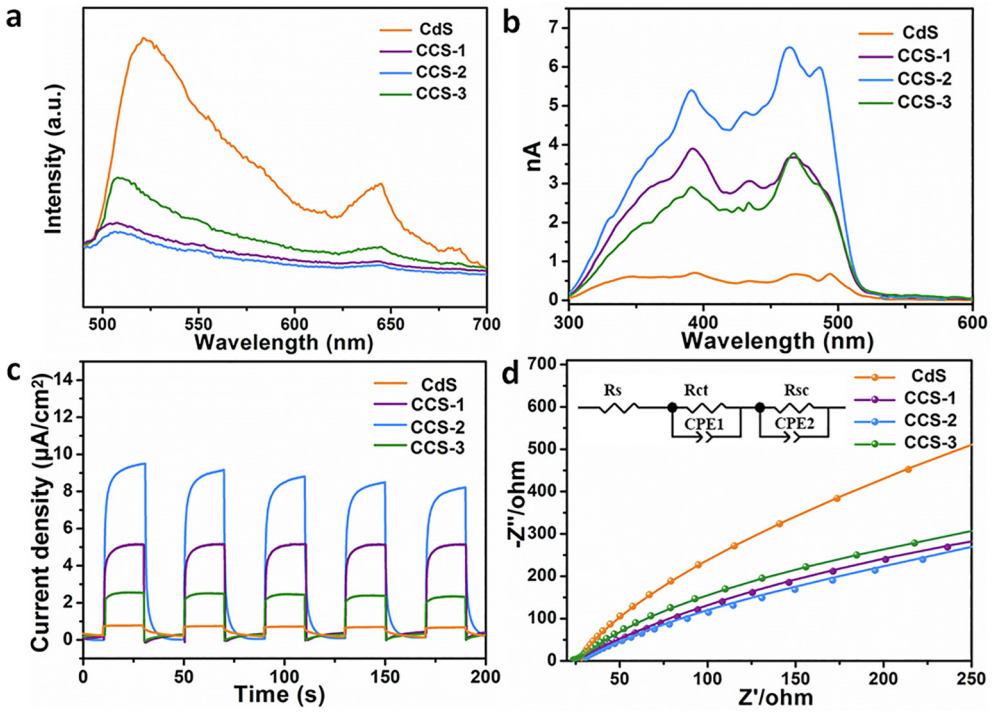

Fig. 7. (a) PL spectra, (b) Surface photocurrent spectrum, (c) Photocurrent response of the different samples under visible-light irradiation (λ > 420 nm), and (d) EIS plots of the as-prepared photocatalysts.

HHNS by growing Co-deficiency $Co_{1-x}S$ HPs on CdS NWs as an efficient visible-light-driven photocatalyst for H_2 production. The loading amount of $Co_{1-x}S$ on an individual CdS NW could be modulated by varying the ratio of ZIF-67 precursor to CdS NWs in sulfidation treatment, and a H_2 production rate of 13.48 mmol g^{-1} h^{-1} has been achieved with the optimized CCS-2 HHNSs under visible-light irradiation. The unique photocatalytic activity is attributed to the coupling of CdS NWs with $Co_{1-x}S$ HPs, which endows the heterostructure with full spectrum response and large surface area with lots of sides, facets to expose active sites. More importantly, the band structure configuration of the heterostructure efficiently facilitate the separation of photo-excited e^--h^+ pairs through the Z-scheme transfer mechanism and lead to strong photoreduction ability due to the lower aligned CB of the $Co_{1-x}S$ HPs. With all these advantages integrated, the CCS HHNSs significantly expedite the photocatalytic H_2 production process. This work provides fresh insights into the construction of Z-Scheme unusual hollow nanostructures as efficient photocatalysts by the means of morphology design and electronic structure modulation.

Declaration of Competing Interest

The authors declare that they have no known competing financial interests or personal relationships that could have appeared to influence the work reported in this paper.

Acknowledgements

Y. Hu acknowledges the financial support from National Natural Science Foundation of China (21671173) and Zhejiang Provincial Ten Thousand Talent Program (2017R52043).

Appendix A. Supplementary data

Supplementary data to this article can be found online at https://doi.org/10.1016/j.cej.2020.125925.

References

[1] M. Luo, Q. Yang, W. Yang, J. Wang, F. He, K. Liu, H. Cao, H. Yan, Defects engineering leads to enhanced photocatalytic H_2 evolution on graphitic carbon nitride-covalent organic framework nanosheet composite, Small 16 (2020) 2001100.
[2] X. Chen, R. Shi, Q. Chen, Z. Zhang, W. Jiang, Y. Zhu, T. Zhang, Three-dimensional porous g-C_3N_4 for highly efficient photocatalytic overall water splitting, Nano Energy 59 (2019) 644–650.
[3] Y. Chao, J. Zheng, H. Zhang, F. Li, F. Yan, Y. Tan, Z. Zhu, Oxygen-incorporation in Co_2P as a non-noble metal cocatalyst to enhance photocatalysis for reducing water to H_2 under visible light, Chem. Eng. J. 346 (2018) 281–288.
[4] A. Fujishima, K. Honda, Electrochemical photolysis of water at a semiconductor electrode, Nature 238 (1972) 37–38.
[5] B. He, H. Liu, Z. Lin, L. Yan, J. Ning, Y. Zhong, C. Zheng, Z. Zhang, Y. Hu, A new photocatalyst based on $Co(CO_3)_{0.5}(OH)$•$0.11H_2O/Bi_2WO_6$ nanocomposites for high-efficiency cocatalyst-free O_2 evolution, Chem. Eng. J. 359 (2019) 924–932.
[6] M. Xu, J. Yang, C. Sun, L. Liu, Y. Cui, B. Liang, Performance enhancement strategies of bi-based photocatalysts: A review on recent progress, Chem. Eng. J. 389 (2020) 124402.
[7] Y. Lu, Y. Huang, Y. Zhang, T. Huang, H. Li, J. Cao, W. Ho, Effects of H_2O_2 generation over visible light-responsive Bi/Bi_2O_2-CO_3 nanosheets on their photocatalytic NO removal performance, Chem. Eng. J. 363 (2019) 374–382.
[8] H. Zhang, C. Guo, J. Ren, J. Ning, Y. Zhong, Z. Zhang, Y. Hu, Beyond CoO_x: a versatile amorphous cobalt species as an efficient cocatalyst for visible-light-driven photocatalytic water oxidation, Chem. Commun. 55 (2019) 14050–14053.
[9] H. Liu, L. Li, C. Guo, J. Ning, Y. Zhong, Y. Hu, Thickness-dependent carrier separation in $Bi_2Fe_4O_9$ nanoplates with enhanced photocatalytic water oxidation, Chem. Eng. J. 385 (2020) 123929.
[10] J. Tang, J.R. Durrant, D.R. Klug, Mechanism of photocatalytic water splitting in TiO_2. reaction of water with photoholes, importance of charge carrier dynamics, and evidence for four-hole chemistry, J. Am. Chem. Soc. 130 (2008) 13885–13891.
[11] X. Wang, S. Shen, Z. Feng, C. Li, Time-resolved photoluminescence of anatase/rutile TiO_2 phase junction revealing charge separation dynamics, Chinese J. Catal. 37 (2016) 2059–2068.
[12] C. Xu, P. Ravi Anusuyadevi, C. Aymonier, R. Luque, S. Marre, Nanostructured materials for photocatalysis, Chem. Soc. Rev. 48 (2019) 3868–3902.
[13] M. Fang, G. Dong, R. Wei, J.C. Ho, Hierarchical nanostructures: design for sustainable water splitting, Adv. Energy Mater. 7 (2017) 1700559.
[14] H. Chen, S. Yang, Hierarchical nanostructures of metal oxides for enhancing charge separation and transport in photoelectrochemical solar energy conversion systems, Nanoscale Horiz. 1 (2016) 96–108.
[15] H.M. Chen, C.K. Chen, R.-S. Liu, L. Zhang, J. Zhang, D.P. Wilkinson, Nano-architecture and material designs for water splitting photoelectrodes, Chem. Soc. Rev. 41 (2012) 5654–5671.
[16] B. You, N. Jiang, M. Sheng, M.W. Bhushan, Y. Sun, Hierarchically porous urchin-like Ni_2P superstructures supported on nickel foam as efficient bifunctional electrocatalysts for overall water splitting, ACS Catal. 6 (2016) 714–721.

[17] H. Wang, L. Zhang, Z. Chen, J. Hu, S. Li, Z. Wang, J. Liu, X. Wang, Semiconductor heterojunction photocatalysts: design, construction, and photocatalytic performances, Chem. Soc. Rev. 43 (2014) 5234–5244.
[18] S. Wang, B.Y. Guan, X.W. Lou, Rationally designed hierarchical N-doped carbon@$NiCo_2O_4$ double-shelled nanoboxes for enhanced visible light CO_2 reduction, Energy Environ. Sci. 11 (2018) 306–310.
[19] S. Wang, Y. Wang, S.-Q. Zang, X.W. Lou, Hierarchical hollow heterostructures for photocatalytic CO_2 reduction and water splitting, Small Methods 4 (2020) 1900586.
[20] D. Zheng, X.-N. Cao, X. Wang, Precise Formation of a Hollow Carbon Nitride Structure with a Janus Surface To Promote Water Splitting by Photoredox Catalysis, Angew. Chem. Int. Ed. 55 (2016) 11512–11516.
[21] B. Qiu, Q. Zhu, M. Du, L. Fan, M. Xing, J. Zhang, Efficient solar light harvesting CdS/Co_9S_8 hollow cubes for Z-scheme photocatalytic water splitting, Angew. Chem. Int. Ed. 56 (2017) 2684–2688.
[22] C. Bie, B. Zhu, F. Xu, L. Zhang, J. Yu, In situ grown monolayer n-doped graphene on cds hollow spheres with seamless contact for photocatalytic CO_2 reduction, Adv. Mater. 31 (2019) 1902868.
[23] S. Wang, B.Y. Guan, X. Wang, X.W.D. Lou, Formation of hierarchical Co_9S_8@$ZnIn_2S_4$ heterostructured cages as an efficient photocatalyst for hydrogen evolution, J. Am. Chem. Soc. 140 (2018) 15145–15148.
[24] S. Wang, B.Y. Guan, Y. Lu, X.W.D. Lou, Formation of Hierarchical In_2S_3-$CdIn_2S_4$ Heterostructured Nanotubes for Efficient and Stable Visible Light CO_2 Reduction, J. Am. Chem. Soc. 139 (2017) 17305–17308.
[25] C. Dong, L. Guo, Y. He, L. Shang, Y. Qian, L. Xu, Ultrafine $Co_{1-x}S$ nanoparticles embedded in a nitrogen-doped porous carbon hollow nanosphere composite as an anode for superb sodium-ion batteries and lithium-ion batteries, Nanoscale 10 (2018) 2804–2811.
[26] H. Wang, Y. Liang, Y. Li, H. Dai, $Co_{1-x}S$-graphene hybrid: a high-performance metal chalcogenide electrocatalyst for oxygen reduction, Angew. Chem. Int. Ed. 50 (2011) 10969–10972.
[27] S. Sun, X. Sun, Y. Liu, J. Peng, Y. Qiu, Y. Xu, J. Zhang, Q. Li, C. Fang, J. Han, Y. Huang, 3D hierarchical porous $Co_{1-x}S$@C derived from a ZIF-67 single crystals self-assembling superstructure with superior pseudocapacitance, J. Mater. Chem. A 7 (2019) 17248–17253.
[28] H. Zhang, P. Zhang, M. Qiu, J. Dong, Y. Zhang, X.W. Lou, Ultrasmall MoO_x clusters as a novel cocatalyst for photocatalytic hydrogen evolution, Adv. Mater. 31 (2019) 1804883.
[29] Y. Hu, X. Gao, L. Yu, Y. Wang, J. Ning, S. Xu, X.W. Lou, Carbon-coated CdS petalous nanostructures with enhanced photostability and photocatalytic activity, Angew. Chem. Int. Ed. 52 (2013) 5636–5639.
[30] S. Wang, J. Li, X. Zhou, C. Zheng, J. Ning, Y. Zhong, Y. Hu, Facile preparation of 2D sandwich-like CdS nanoparticles/nitrogen-doped reduced graphene oxide hybrid nanosheets with enhanced photoelectrochemical properties, J. Mater. Chem. A 2 (2014) 19815–19821.
[31] B. He, R. Liu, J. Ren, C. Tang, Y. Zhong, Y. Hu, One-step solvothermal synthesis of petalous carbon-coated Cu^+-doped CdS nanocomposites with enhanced photocatalytic hydrogen production, Langmuir 33 (2017) 6719–6726.
[32] C. Zhang, H. Liu, W. Wang, H. Qian, S. Cheng, Y. Wang, Z. Zha, Y. Zhong, Y. Hu, Scalable fabrication of $Zn_xCd_{1-x}S$ double-shell hollow nanospheres for highly efficient hydrogen production, Appl. Catal. B-Environ. 239 (2018) 309–316.
[33] Y.M. Wang, Z.Y. Wu, L.Y. Shi, J.H. Zhu, Rapid functionalization of mesoporous materials: directly dispersing metal oxides into As-prepared SBA-15 occluded with template, Adv. Mater. 17 (2005) 323–327.
[34] J. Zhu, Z. Ren, S. Du, Y. Xie, J. Wu, H. Meng, Y. Xue, H. Fu, Co-vacancy-rich $Co_{1-x}S$ nanosheets anchored on rGO for high-efficiency oxygen evolution, Nano Res. 10 (2017) 1819–1831.
[35] Y. Liu, H. Cheng, M. Lyu, S. Fan, Q. Liu, W. Zhang, Y. Zhi, C. Wang, C. Xiao, S. Wei, B. Ye, Y. Xie, Low overpotential in vacancy-rich ultrathin $CoSe_2$ nanosheets for water oxidation, J. Am. Chem. Soc. 136 (2014) 15670–15675.
[36] H. Liu, K. Tian, J. Ning, Y. Zhong, Z. Zhang, Y. Hu, One-step solvothermal formation of Pt nanoparticles decorated Pt^{2+}-doped α-Fe_2O_3 nanoplates with enhanced photocatalytic O_2 evolution, ACS Catal. 9 (2019) 1211–1219.
[37] D.A. Reddy, H. Park, M. Gopannagari, E.H. Kim, S. Lee, D.P. Kumar, T.K. Kim, Designing CdS mesoporous networks on Co-C@Co_9S_8 double-shelled nanocages as redox-mediator-free Z-scheme photocatalyst, ChemSusChem 11 (2018) 245–253.
[38] J. Low, B. Dai, T. Tong, C. Jiang, J. Yu, In Situ Irradiated X-Ray Photoelectron Spectroscopy Investigation on a Direct Z-Scheme TiO_2/CdS Composite Film Photocatalyst, Adv. Mater. 31 (2019) 1802981.
[39] X. Liu, G. Dong, S. Li, G. Lu, Y. Bi, Direct observation of charge separation on anatase TiO_2 crystals with selectively etched 001 facets, J. Am. Chem. Soc. 138 (2016) 2917–2920.
[40] H. Luo, B. Wang, T. Liu, F. Jin, R. Liu, C. Xu, C. Wang, K. Ji, Y. Zhou, D. Wang, S. Dou, Hierarchical design of hollow Co-Ni LDH nanocages strung by MnO_2 nanowire with enhanced pseudocapacitive properties, Energy Storage Mater. 19 (2019) 370–378.
[41] M. Li, S. Yu, H. Huang, X. Li, Y. Feng, C. Wang, Y. Wang, T. Ma, L. Guo, Y. Zhang, Unprecedented eighteen-faceted BiOCl with a ternary facet junction boosting cascade charge flow and photo-redox, Angew. Chem. Int. Ed. 58 (2019) 9517–9521.
[42] P. Wang, T.-F. Xie, H.-Y. Li, L. Peng, Y. Zhang, T.-S. Wu, S. Pang, Y.-F. Zhao, D.-J. Wang, Synthesis and plasmon-induced charge-transfer properties of monodisperse gold-doped titania microspheres, Chem. Eur. J. 15 (2009) 4366–4372.
[43] Y. Zhao, Y. Zhao, G.I.N. Waterhouse, L. Zheng, X. Cao, F. Teng, L.-Z. Wu, C.-H. Tung, D. O'Hare, T. Zhang, Layered-double-hydroxide nanosheets as efficient visible-light-driven photocatalysts for dinitrogen fixation, Adv. Mater. 29 (2017) 1703828.
[44] W. Zhong, S. Shen, M. He, D. Wang, Z. Wang, Z. Lin, W. Tu, J. Yu, The pulsed laser-induced Schottky junction via in-situ forming Cd clusters on CdS surfaces toward efficient visible light-driven photocatalytic hydrogen evolution, Appl. Catal. B-Environ. 258 (2019) 117967.
[45] X. Zhang, M. Ge, J. Dong, J. Huang, J. He, Y. Lai, Polydopamine-inspired design and synthesis of visible-light-driven Ag NPs@C@elongated TiO_2 NTs core-shell nanocomposites for sustainable hydrogen generation, ACS Sustain. Chem. Eng. 7 (2019) 558–568.